Size-Dependent Fracture of Silicon Nanoparticles During Lithiation

Xiao Hua Liu,[†] Li Zhong,[‡] Shan Huang,[§] Scott X. Mao,[‡] Ting Zhu,[§,*] and Jian Yu Huang[†,*]

[†]Center for Integrated Nanotechnologies (CINT), Sandia National Laboratories, Albuquerque, New Mexico 87185, United States, [‡]Department of Mechanical Engineering and Materials Science, University of Pittsburgh, Pittsburgh, Pennsylvania 15261, United States, and [§]Woodruff School of Mechanical Engineering, Georgia Institute of Technology, Atlanta, Georgia 30332, United States

Lithium ion batteries (LIBs) are widely used as power devices for portable electronics. For more demanding applications such as powering electric vehicles, LIBs with radically improved energy density and power capability are highly desirable.[1−4] Silicon represents one of the most promising anode materials for the next-generation LIBs, as it has a Li storage capacity (3579 mAh/g for $Li_{15}Si_4$ at room temperature)[5−8] about 10 times larger than that of the carbonaceous anodes (372 mAh/g for LiC_6) used in commercial LIBs. However, Si undergoes ∼280% volumetric expansion when alloying with Li to form the $Li_{15}Si_4$ phase at room temperature.[7,9] Pulverization and the resultant loss of electrical contact have been recognized as one of the major causes of rapid capacity fading in Si-based electrodes, hindering application of such alloying anodes in LIBs.[5,10−13]

To mitigate the adverse mechanical effects accompanying electrochemical lithiation, nanostructured Si and composite Si-based electrodes have been intensively studied;[5,12,14−20] they have shown improved performance, presumably due to the small sizes that enable fast Li transport and facile strain relaxation.[15,21] However, one of the fundamental questions remains unclear—what is the critical size below which the lithiation-induced strain can be accommodated without fracture in a Si electrode? Recently, Ryu *et al.* reported that Si nanowires with diameters less than 300 nm could not fracture even if pre-existing cracks were present.[22] In contrast, *in situ* experiments inside a transmission electron microscope (TEM) revealed the fracture of the single Si nanowire by self-splitting into two subwires during lithiation.[9] Therefore, determining how a crack initiates and identifying a critical size for averting a fracture in Si nanomaterials could be of both great fundamental and technological interest, considering that

ABSTRACT
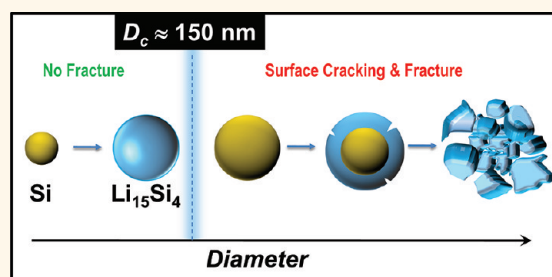
Lithiation of individual silicon nanoparticles was studied in real time with *in situ* transmission electron microscopy. A strong size dependence of fracture was discovered; that is, there exists a critical particle diameter of ∼150 nm, below which the particles neither cracked nor fractured upon first lithiation, and above which the particles initially formed surface cracks and then fractured due to lithiation-induced swelling. The unexpected surface cracking arose owing to the buildup of large tensile hoop stress, which reversed the initial compression, in the surface layer. The stress reversal was attributed to the unique mechanism of lithiation in crystalline Si, taking place by movement of a two-phase boundary between the inner core of pristine Si and the outer shell of amorphous Li—Si alloy. While the resulting hoop tension tended to initiate surface cracks, the small-sized nanoparticles nevertheless averted fracture. This is because the stored strain energy from electrochemical reactions was insufficient to drive crack propagation, as dictated by the interplay between the two length scales, that is, particle diameter and crack size, that control the fracture. These results are diametrically opposite to those obtained previously from single-phase modeling, which predicted only compressive hoop stress in the surface layer and thus crack initiation from the center in lithiated Si particles and wires. Our work provides direct evidence of the mechanical robustness of small Si nanoparticles for applications in lithium ion batteries.

Si-based electrodes hold the promise of markedly improving the capacity of LIBs.[5]

Here we report the lithiation behavior of *individual* spherical Si nanoparticles (SiNPs), as a model system, with sizes varying from a few tens of nanometers to several micrometers. Their lithiation behavior was studied *in situ* inside a TEM,[3,8,9,21,23−29] either by an electrochemical lithiation method in the solid-cell configuration (Supporting Information,
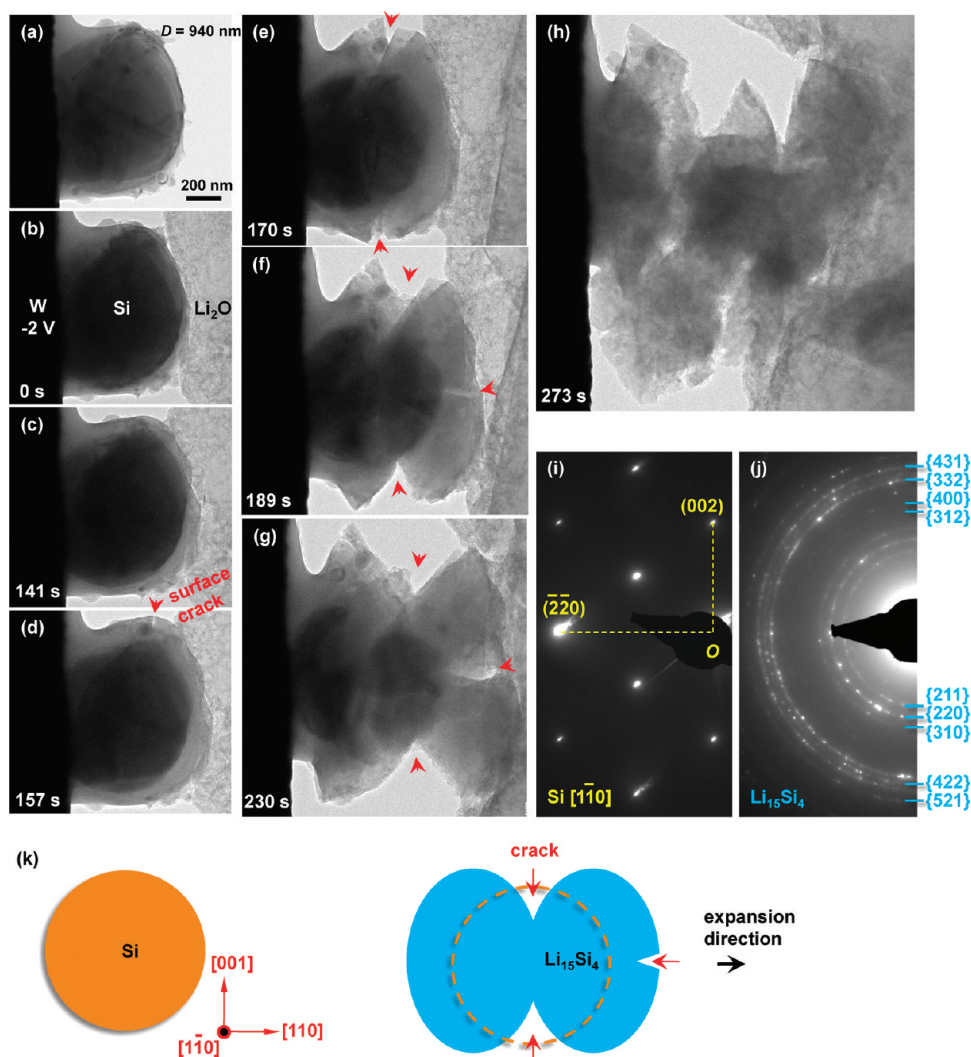
Figure 1. Surface cracking and fracture of a large silicon nanoparticle (SiNP) during electrochemical lithiation. (a) Pristine SiNP with a diameter of ∼940 nm. (b−h) Crack nucleation and fracture of the SiNP in the lithiation process. After the Li$_2$O/Li electrode contacted the SiNP sitting on the W electrode, a potential of −2 V was applied to the W electrode with respect to the Li metal (b). The lithiation occurred on the particle surface and proceeded inward as the gray-contrasted Li$_x$Si shell was thickened. When the shell thickness reached ∼150 nm, the first crack emerged near the surface, as marked by the red arrowhead (d). More cracks nucleated and propagated along different directions upon further lithiation (e−g), and finally the particle exploded into many tiny pieces (h). (i,j) Electron diffraction patterns (EDPs) showing the phase transformation from single crystalline Si (i) to polycrystalline Li$_{15}$Si$_4$ after lithiation (j). (k) Schematic illustration showing the crystallography, expansion, and crack formation. The swelling was along Si ⟨110⟩ directions.

Figure S1a),[3,9,26−28] or by the constraint-free chemical lithiation method assisted by electron-beam-induced decomposition of Li$_2$O (Figure S1b).[30−32] By directly observing the lithiation process of the SiNPs, we found that a SiNP can be lithiated without cracking when the diameter (D) is below the critical size, $D_c \approx$ 150 nm. However, large SiNPs above this critical size consistently crack into pieces upon lithiation. This size effect is analyzed on the basis of a model of stress generation at and behind the moving two-phase boundary during lithiation, and the origin of size effects is attributed to the particle-size-dependent crack extension driving force in lithiated NPs. Our findings provide new insights into the electrochemical-mechanical coupling during the Si−Li alloying process and shed light on the mitigation

of mechanical failures and the design of high-capacity Si electrodes for advanced LIBs.

RESULTS AND DISCUSSION

Figure 1 and Movie S1 (Supporting Information, nn204476h_si_002.avi) show the cracking and fracture of a large SiNP during the electrochemical lithiation process. The pristine SiNP had a diameter of 940 nm (Figure 1a). As the front surface of the Li$_2$O layer touched the SiNP (Figure 1b), a −2 V bias was applied.[9] Lithiation occurred on all surfaces within 2 min (Figure 1c), indicating fast lithium diffusion on the Si surface. The radial flow of Li from the surface toward the center of the SiNP resulted in a gray-contrasted shell enclosing a dark Si core. When the Li$_x$Si shell
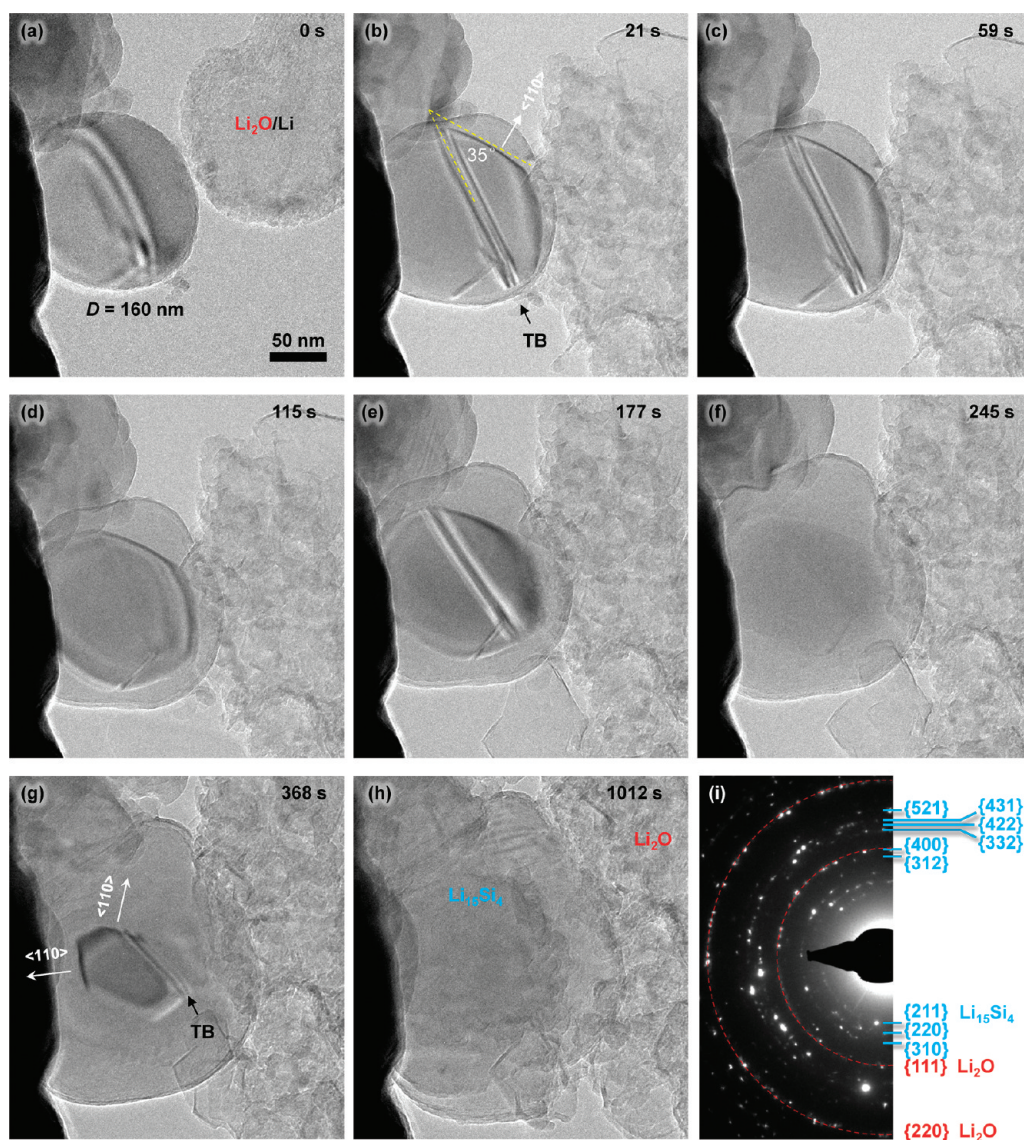
Figure 2. Electrochemical lithiation of a small SiNP around the critical size showing no fracture. (a) Pristine SiNP with a diameter of about 160 nm. (b–g) Steady lithiation stage without cracking. There was a twin boundary (TB) in the center of the SiNP. Fast swelling along ⟨110⟩ resulted in a bump on the flat (110) plane, which formed a 35° angle with the TB (b). Anisotropic lithiation led to formation of the faceted Si core during the lithiation process (g). (h) Morphology of the fully lithiated particle. The electron beam was blanked during the lithiation process except for a short exposure for imaging. (i) EDP from the fully lithiated particle confirming the formation of polycrystalline $Li_{15}Si_4$ phase (blue lines and indices). The Li_2O phase showing up in the EDP was from the adjacent Li_2O layer (red dashed arcs and indices).

reached the thickness of ∼150 nm, a crack nucleated near the surface (Figure 1d), and propagated inward quickly as the lithiation continued (Figure 1e). In the meantime, new cracks emerged at different locations on the particle (Figure 1e,f). The growth of multiple cracks at different locations eventually led to fracture of the particle into several tiny pieces (Figure 1g,h). The electron diffraction patterns (EDPs) confirmed the phase transformation from single crystalline Si (Figure 1i) to polycrystalline $Li_{15}Si_4$ (Figure 1j) after lithiation.[8,9] This is consistent with the previously reported phase transformations of Si during lithiation; that is, crystalline Si first undergoes an amorphization process to form a Li_xSi alloy, which then crystallizes to

$Li_{15}Si_4$ upon full lithiation.[6−9,33] Figure 1k illustrates the crystallography and mechanical deformation during the lithiation process. Our previous studies have shown that lithiation-induced swelling is preferably along the ⟨110⟩ directions in Si nanowires,[9] which is consistent with the anisotropic expansion of the SiNP.

Intriguingly, smaller SiNPs did not crack during the electrochemical lithiation (Figures 2−3 and Supporting Information, Movie S2, nn204476h_si_003.avi). Figure 2 shows the electrochemical lithiation process of a SiNP with a 160 nm diameter around the critical size D_c (Figure 2a). There was a twin boundary in the center of the SiNP. The preferred expansion along the ⟨110⟩
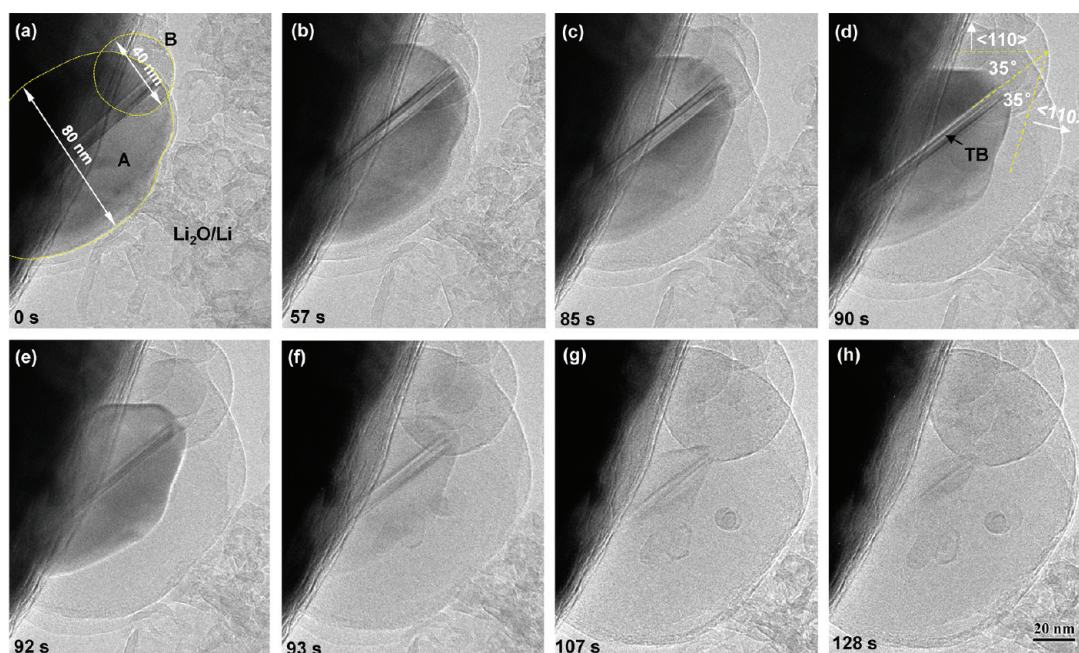
Figure 3. Electrochemical lithiation of two small SiNPs below the critical size and without fracture. (a) Two pristine SiNPs, marked by "A" and "B" with diameters of 80 and 40 nm, respectively. There was a twin boundary (TB) in the center of Particle A. (b−h) Morphology evolution during lithiation. Fast lithiation was seen along the ⟨110⟩ directions in particle A (d), forming 35° angles between the flat {110} planes and the (111) TB in the center (d). (h) No cracking and fracture was seen for the two lithiated nanoparticles. The lithiation completed in about 2 min, but no cracks formed despite the high lithiation rate.

direction resulted in a bump and a flat (110) facet with a characteristic 35° angle to the twin boundary (Figure 2b). The morphological evolution during lithiation exhibited anisotropy (Figure 2a−g), as evidenced by the formation of the faceted Si core and the bumped shell structures (Figure 2g), which were in contrast to the round shape of the pristine particle (Figure 2a). The SiNP did not crack when the Si core disappeared, and the particle diameter expanded to about 255 nm after lithiation (Figure 2h); this corresponds to ∼300% volume expansion, and is close to the theoretical limit at full lithiation. The EDP from the fully lithiated particle confirmed that the polycrystalline $Li_{15}Si_4$ phase was obtained again (Figure 2i), the same as that seen for large particles in Figure 1j except for the obvious rings from the adjacent Li_2O (marked by the red arcs in Figure 2i). Figure 3 shows the lithiation of other two SiNPs (marked as A and B) with diameters of ∼80 and 40 nm, respectively, which are significantly below the critical size D_c (Figure 3a). Both particles underwent the core−shell lithiation process (Figure 3b−g) and remained unbroken after lithiation (Figure 3h). There was also a twin boundary in the center of the bigger particle A (Figure 3d). Preferential lithiation along the ⟨110⟩ directions was seen with flat {110} planes as the Li_xSi/Si phase boundaries (Figure 3d). The phase boundaries and the twin boundary formed the characteristic 35° angle between the (110) and (111) planes. The smaller SiNP B did not directly contact the Li_2O layer; thus it was freestanding without external constraints. Lithiation was then

accomplished with lithium transport through the Li_xSi shell formed on particle A. This indicates that the lithiation and associated deformation are dependent on the particle size rather than on the specified lithiation conditions. It is worth noting that the twinned structures were frequently observed in Si nanoparticles, but they did not show detectable influence on the lithiation or fracture behaviors.

To further exclude any influence from the constraints of the tungsten and lithium electrodes, chemical lithiation of *free-standing* SiNPs was also conducted (see details in the experimental section and in Supporting Information), and this revealed the same size dependence of fracture during lithiation. For a 620-nm SiNP (Figure 4), lithiation resulted in a sequential morphology evolution of the core−shell structure (Figure 4a,b) through intermediate cracking (Figure 4b−d) and to the final fractured structure (Figure 4e). The fully lithiated phase was also crystalline $Li_{15}Si_4$ (Figure 4f). In contrast, an 80-nm SiNP uniformly expanded to 130 nm after lithiation (Figure 5), without any cracking or fracture despite the volumetric expansion of around 300%. The SiNP was suspended and connected to the lithium source through the Si nanowire, which also served as the Li diffusion path (Figure 5a). More examples are given in the Supporting Information, showing a clear size dependence on the lithiation-induced fracture of SiNPs (Figures S2−S4). The fully lithiated phase for all the SiNPs was always the crystalline $Li_{15}Si_4$.

Statistics for the fracture behavior of many SiNPs showed a critical size, $D_c ≈ 150 ± 10$ nm, above which
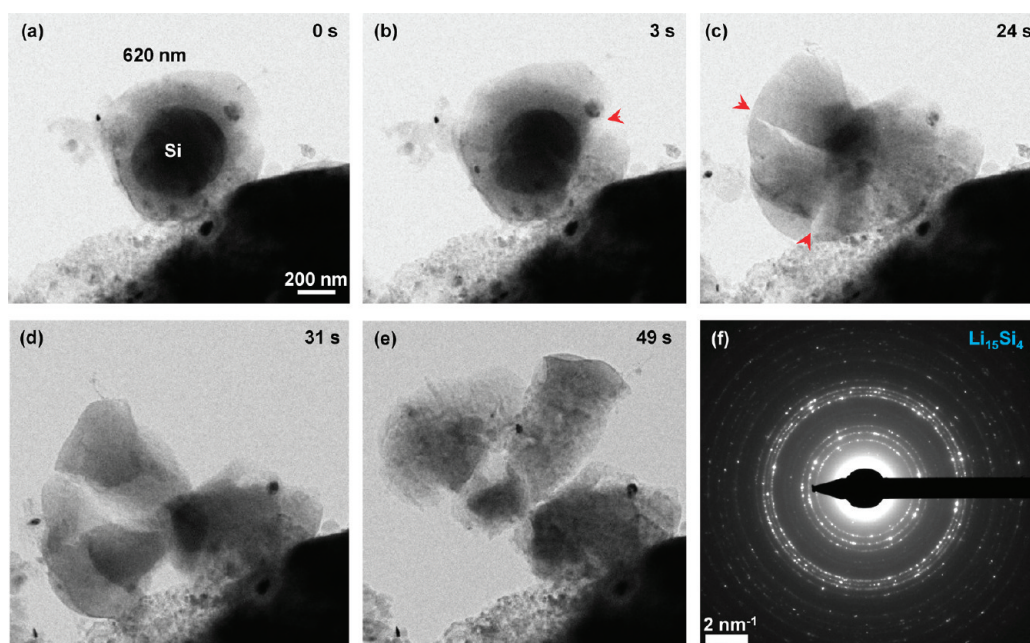
Figure 4. Fast fracture of a free-standing 620-nm SiNP during chemical lithiation in one minute. (a–e) Time sequence of crack initiation and growth. (f) EDP indicating formation of polycrystalline Li$_{15}$Si$_4$ as the fully lithiated phase.
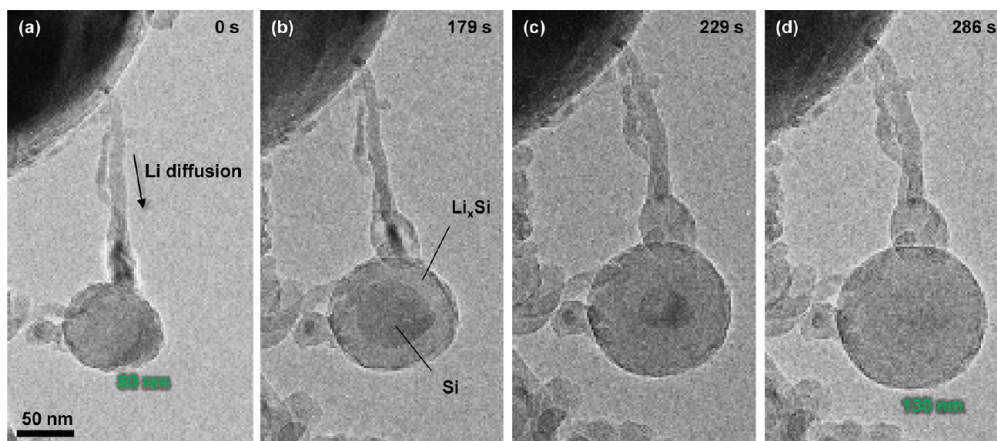

Figure 5. Chemical lithiation of another Si nanoparticle without cracking. (a) A pristine Si nanoparticle with D = 80 nm. (b,c) Core−shell structure during gradual lithiation from the surface to the center. The nanowire hanging the SiNP provided the Li diffusion path. (d) Completion of lithiation without cracking. The diameter of the lithiated nanoparticle was 130 nm, corresponding to a volumetric expansion around 300%. The lithiation completed in about 7 min, but no crack was observed despite the high lithiation rate.

cracking occurred upon the first lithiation and below which cracking was not observed (Figure 6). We note that the charging-rate-dependent fracture has been suggested for Si electrodes (*i.e.*, faster lithiation rates are thought to lead to more severe crack formation).[34] However, in our experiments we did not observe any correlation between the lithiation rate and fracture— for instance, fast lithiation did not result in cracking among small SiNPs (Figures 3 and 5, Supporting Information Figure S4) and slow lithiation did not prevent a large SiNP from cracking either (Figure S2). Besides, the first surface cracks usually emerged when the Li$_x$Si shell thickness (denoted as t) reached 100–200 nm, and this observation is in good agreement with

the observed critical size D_c of about 150 nm. In a large size range of 150–2000 nm, the ratio of t/D (t denoting the Li$_x$Si shell thickness when the first crack appeared) increases with decreasing D (Figure 6), which is consistent with the final entrance into the nonfracture zone. It appears that the fracture of SiNPs during lithiation is controlled by the particle size.

To understand the particle size effect on fracture, the first priority is to know how the mechanical stresses were generated and distributed during progressive lithiation. Existing models of diffusion-induced stress considered Li diffusion in a single-phase material and thus predicted the development of hoop compression in the surface layer (*i.e.*, suppressing the fracture
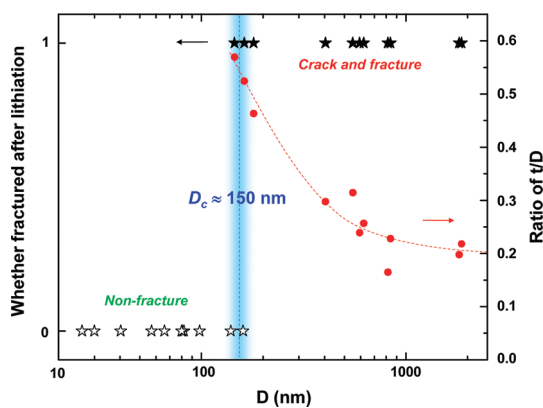
Figure 6. Statistics showing the critical size (D_c) around 150 nm. In the nonfracture zone ($D < D_c$), the SiNPs did not crack or fracture upon first lithiation (open stars). When D was larger than D_c, the SiNPs always cracked and fractured (solid stars). With decreasing D, the ratio of t/D (t, the Li$_x$Si shell thickness when first crack appeared) monotonically increases from about 0.2 to 0.6 (red dots), indicating a relatively delayed crack event in smaller SiNPs, consistent with the final entrance into the nonfracture zone.

therein) and tension in the center where fracture was believed to first occur.[20,34,35] This contrasts with our *in situ* TEM observations of fracture initiation from the particle surface (for instance, Figure 1d). To resolve this inconsistency, it is critical to appreciate the difference in stress generation within a spherical particle controlled by the radial Li diffusion in a *single-phase* material as opposed to that by motion of a *two-phase* interface. Taking advantage of the large contrast in electron transparency between the crystalline and amorphous phases, our *in situ* TEM experiments clearly revealed the development of a core−shell structure, consisting of a two-phase interface that separated an inner core of crystalline Si with an outer shell of amorphous Li$_x$Si ($x \approx 3.75$). TEM observations indicated that the two-phase interface is both structurally and chemically sharp. This suggested that the two phases did not transform continuously into each other with changing composition; that is, the solubility gap Δx is large at room temperature. When such a two-phase interface moved from the surface to the center of a particle, the lithiation-induced deformation ($\sim$300% volume strain) occurred dominantly at the interface, across which the lithiation concentration changed sharply, that is, from $x \approx 0$ to 3.75. The local strain compatibility dictated that the hoop stress at the interface should be compressive, as shown in Figure 7a (the details of the mechanics model and finite element simulation have been described in the Supporting Information). Furthermore, if such a moving interface was planar, the lithiated material behind it would not further deform as the lithiation proceeded. In contrast, the core−shell interface was curved, such that the lithiation-induced radial expansion at the moving interface continuously pushed out the materials in its wake, leading to the hoop stretch in the outer

layer in a fashion similar to the way the inflation of a balloon causes its wall to stretch. This curvature effect resulted in reversal of the initial hoop compression into tension in the surface layer, as shown in Figure 7b. The Supporting Information provides further discussion of this stress reversal response in terms of the two-stage stressing history of a representative material element in the surface layer. Notably, the stress reversal was strongly encouraged by the two-phase lithiation mechanism which is unlikely to be sensitive to the rate of lithiation, since the sharp two-phase interface has also been observed in Si thin film subjected to a very slow lithiation rate ($\sim$1 nm/min, as opposed to $\sim$100 nm/min in this work).[36]

To understand why the results from the two-phase modeling are different from the previous studies that predicted only hoop compression in the surface layer, we note that in the model of Li diffusion in a single-phase material, the Li concentration increases gradually from the particle center to its surface. For two neighboring material elements, the one at a slightly larger radial distance always has a higher Li concentration than its neighbor, so as to drive the inward diffusion of Li. The concentration difference can result in strain mismatch, and therefore an additional compressive hoop stress in the former element relative to the latter. This mechanism of stress generation arises due to the so-called "differential concentration" effect. Now let us focus on the stress history of a representative material element, called B, in the surface layer. As lithiation proceeds, the Li concentration in element B continuously increases, and so does the hoop compression due to the "differential concentration" effect. On the other hand, a tensile hoop stress in element B could be induced by the "push-out" effect due to the volume expansion of materials at smaller radial distances relative to element B. However, this tension is insufficient to offset the continuously increasing compressive stress caused by the differential concentration effect, such that the hoop compression is retained within the surface layer in the single-phase model. This is in contrast to our two-phase model, where stressing due to the differential concentration effect is only significant near the phase boundary, and the push-out effect is large enough to reverse the initial hoop compression into tension in the surface layer. Clearly, the large hoop tension in the outer layer of the particle provided the main driving force of surface cracking.

The foregoing stress analysis provides a physical basis for understanding size-dependent fracture in lithiated nanoparticles.[37−39] The essential point is that the crack extension is facilitated not only by the high stresses but also by the size of the high-stress region that is controlled by the interplay between two length scales, particle diameter and flaw size. More specifically, when a crack-like flaw of length a is formed in a large particle, near the crack faces the lithiation-induced tensile
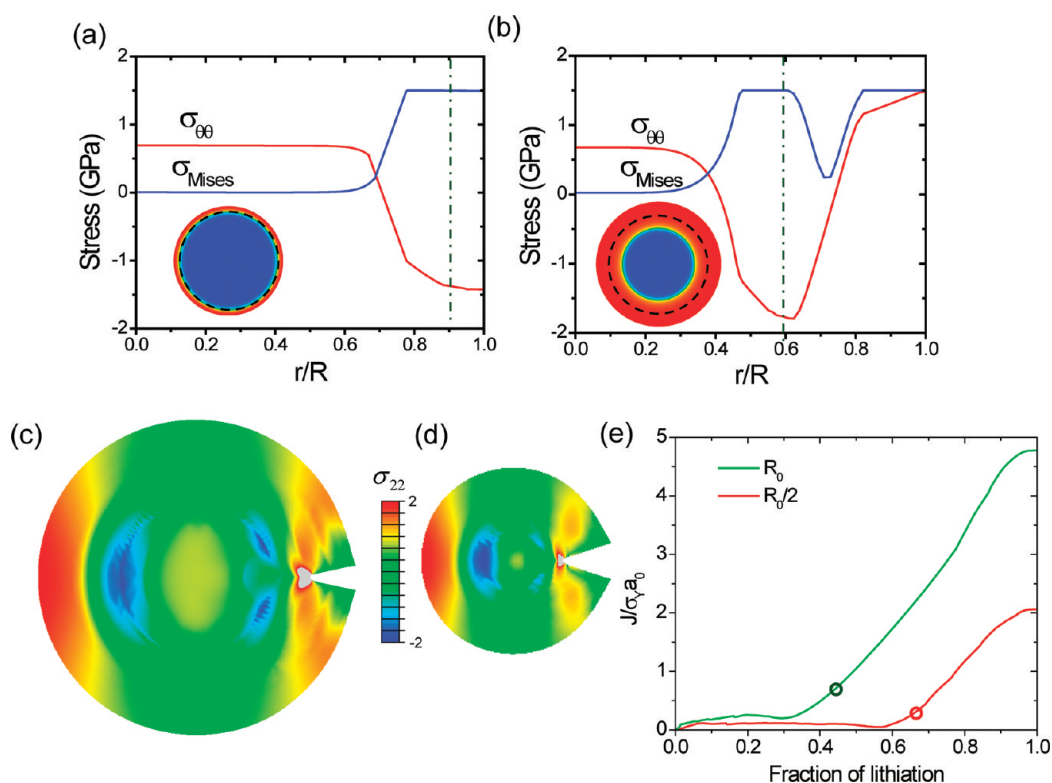
Figure 7. Modeling of lithiation and stress generation in a SiNP. (a) Radial distribution of the hoop stress $\sigma_{\theta\theta}$ and von Mises stress σ_{Mises}, the dot−dash line indicates the location of the reaction front, that is, core−shell interface, and the radial distance r is normalized by the current outer radius R of the partially lithiated particle. Plastic yielding (*i.e.*, σ_{Mises} equals to the yield stress of 1.5 GPa) is attained in the outer layer, where the hoop stress is compressive. The inset gives the contour of Li concentration, c, normalized by the maximum value at the fully lithiated state (blue, $c = 0$; red, $c = 1$), showing the core−shell structure. The particle prior to lithiation is indicated by the dashed line. **(b)** Stress distribution at a later stage of lithiation, with the same representation scheme as that in panel a. Notice that the hoop tension is developed in the outer layer, and it is larger than that in the center, facilitating fracture from the surface. **(c,d)** Stress relaxation due to surface cracking in a simplified geometry of a wire with the cross section of radii R_0 and $R_0/2$, respectively; the crack length $a_0 = 0.1R_0$ in both cases. For each cross section, comparison of the stress distribution between the (left) uncracked part with the (right) cracked part reveals the size scale of the stress relief area, which depends on the cross-sectional radius. This results in the size-dependent energy release rate to drive crack extension. **(e)** *J*-integral near the crack tip as a function of fraction of lithiation, defined as the ratio between the thicknesses of the lithiated shell to the current radius of the cross section. Green and red circles correspond to *J*-integral of the cracked state in panels c and d, respectively.

stress is relaxed to zero, and far from them it is unchanged. Approximately, a region of size a around the crack is relieved of its elastic energy, and this energy release is insensitive to the particle size. However, when the particle size is reduced to be comparable to the crack size, the region of zero stress near the crack faces and accordingly that of elastic energy relief become dependent on the particle size. The smaller the particle is, the less the stress-relief volume (Figure 7c *versus* Figure 7d), and the lower the elastic energy release. A crack will not extend if the driving force of strain energy release rate is less than the resistance of surface energy. This explains the observation of the critical particle size in averting fracture during our lithiation experiments.

To corroborate the above analysis, we used the nonlinear fracture mechanics approach to evaluate the size effect on the *J*-integral, which is an effective measure of crack extension driving force when plastic deformation is involved.[40] The results clearly show a strong size dependence of the *J*-integral, that is, the

strain energy release rate of fracture (Figure 7e), while a quantitative prediction of critical sizes warrants further study when the experimental values of lithiation-dependent diffusion and elastic-plastic properties become available.[41] Moreover, it is interesting to develop mechanistic models to understand the effect of anisotropic swelling[9] on fracture.

Our findings have implications for the SiNP-based LIB electrodes, as well as for other high-capacity nanomaterial electrodes. First, fracture occurs even at the first lithiation process for big particles, rather than in the course of multiple charge/discharge cycles, as widely believed. Second, composite electrodes made of small SiNPs with $D < D_c$ and some elastomeric binder (and other possible additives) may retain their integrity during the "breathing" (reversible volume change) of the active material in cycles.[10,11,42] For alloying anodes based on Si, tin (Sn), or germanium (Ge), large volume change always accompanies the desired high capacity. However, determining the "no-fracture" size is the first

important step toward nanoengineering the electrodes to mitigate the adverse mechanical effects.

CONCLUSION

In summary, we show experimentally a strong particle-size-dependent fracture behavior of Si nanoparticles during the first lithiation; that is, there exists a critical particle size of ~150 nm below which cracking did not occur, and above which surface cracking and particle fracture took place upon lithiation. The unexpected surface cracking is attributed to the development of hoop tension in the surface layer, resulting from a unique lithiation mechanism in crystalline Si nanoparticles by means of motion of a two-phase interface. The strong size-dependence of fracture arises due to an insufficient amount of strain energy release to drive crack propagation in small-sized nanoparticles, as dictated by the interplay between the two length scales, that is, particle diameter and flaw size, that control the fracture. The physics of stress generation, surface cracking, and size effect on fracture revealed in this work have general implications for building reliable lithium ion batteries through size optimization of electrode materials. Furthermore, it may motivate similar studies for a wide range of high-capacity electrode materials (e.g., Ge, Sn, etc.) that involve extremely large swelling (more than 100%) during electrochemical reactions.

EXPERIMENTAL AND MODELING DETAILS

***In Situ* TEM Experiments.** The experimental setup is schematically illustrated in Supporting Information, Figure S1. All the tests were conducted at room temperature (~20 °C). A 250-μm-thick tungsten rod was cut to produce a clean and fresh cross section, which was then used to scratch the Li metal surface to fetch some fresh Li. A conformal coating layer of Li (~300 μm in diameter and ~50 μm in thickness) on one end of the W rod served as the reference electrode and lithium source. The W rod was then mounted onto the Nanofactory TEM-scanning tunneling microscopy (STM) holder by a screw for reliable mechanical and electrical connection. SiNPs were randomly dispersed onto a W rod as the working electrode by directly touching SiNPs powder with a freshly cut W rod. A Li$_2$O layer formed on the Li metal during the sample transfer process and served as the solid electrolyte. The fracture behavior of individual SiNPs was studied under both the electrochemical and chemical lithiation conditions. In the case of electrochemical lithiation (Supporting Information, Figure S1a), a bias of −2 V was applied on the SiNPs against the Li counter-electrode to promote Li ion transport through the Li$_2$O layer for the electrochemical lithiation.[9,26] The electron beam intensity was minimized to avoid possible beam effects, that is, using a weak beam <1 A/cm^2 and blocking the beam except for imaging. In the case of chemical lithiation (Supporting Information, Figure S1b), no voltage was applied, and the electron beam dosage rate was tuned high enough (~100 A/cm^2) to induce Li$_2$O decomposition, such that reactive elemental Li was produced to lithiate the adjacent SiNPs. The advantage of the chemical lithiation method is that the SiNPs were lithiated without the external constraints that otherwise exist in the electrochemical lithiation, as these might change the deformation and fracture behavior of the NPs during lithiation. Nevertheless, the results from both the electrochemical and chemical lithiation methods showed the same size dependence, indicating that it is intrinsic to the Li−Si alloying process and nanoparticle geometry.

Modeling. To gain insights into the stress development during lithiation, we have simulated the coevolving processes of phase evolution and stress generation. The time evolution of the two-phase microstructure is modeled by using a nonlinear diffusion model. Specifically, the concentration of Li, c, is governed by the standard diffusion equation. It is normalized by the Li concentration at the fully lithiated state, such that c varies between 0 and 1. To capture the coexistence of Li-poor and Li-rich phases, we assume that the diffusivity D is nonlinearly dependent on c. Note that our diffusion simulations mainly serve to generate a sequence of core−shell two-phase structures for the stress analyses, rather than provide a precise description of the dynamic lithiation process that would be difficult due to lack of experimental measurements for model calibration. To this end, we take a simple nonlinear function $D = D_0[1/(1 − c) − 2\Omega c]$, where D_0 is the diffusivity constant and Ω is tuned to control the concentration profile near the reaction front. In diffusion simulations, the normalized Li concentrations behind the reaction front can quickly attain the high values (slightly below 1), while those ahead of the front remain nearly zero. This produces a sharp reaction front that is consistent with experimental observation, thereby providing a basis of further stress analysis. It should be noted that a small gradient of lithium concentration still exists behind the reaction front, so that Li can diffuse through the lithiated shell continuously to reach and move forward the reaction front toward the center of the particle. Finally, we emphasize again that the above nonlinear diffusivity function is empirical, and taken as a numerical convenience for generating a sharp phase boundary for stress analyses. The mechanistically based model is needed to describe the motion of phase boundary and Li diffusion in each phases in the future study. The particle is initially pristine and subjected to a constant Li flux I_0 at the surface.

We adopt an elastic and perfectly plastic model to describe the lithiation-induced deformation. The total strain rate, $\dot{\varepsilon}_{ij}$, is taken to be the sum of three contributions, $\dot{\varepsilon}_{ij} = \dot{\varepsilon}_{ij}^c + \dot{\varepsilon}_{ij}^e + \dot{\varepsilon}_{ij}^p$. Here, $\dot{\varepsilon}_{ij}^c$ denotes the chemical strain rate caused by lithiation and is proportional to the rate of the normalized Li concentration $\dot{c}$. That is, $\dot{\varepsilon}_{ij}^c = \beta_{ij}\dot{c}$, where β_{ij} is the lithiation expansion coefficient and c varies between 0 (e.g., pristine Si) and 1 (e.g., fully lithiated Li$_{3.75}$Si). In the above definition of total strain rate, $\dot{\varepsilon}_{ij}^e$ denotes the elastic strain rate and obeys Hooke's law, $\dot{\varepsilon}_{ij}^e = {}^1/_E[(1 + v)\dot{\sigma}_{ij} − v\dot{\sigma}_{kk}\delta_{ij}]$, where E is Young's modulus, v is Poisson's ratio, $\delta_{ij} = 1$ when $i = j$ and $\delta_{ij} = 0$ otherwise, repeated indices mean summation. The plastic strain rate, $\dot{\varepsilon}_{ij}^p$, obeys the classic J_2-flow rule. That is, plastic yielding occurs when the von Mises equivalent stress, $\sigma_{eq} = (3\sigma'_{ij}\sigma'_{ij}/2)^{1/2}$, equals the yield strength σ_Y, where $\sigma'_{ij} = \sigma_{ij} − \sigma_{kk}\delta_{ij}/3$ is the deviatoric stress. In addition, the plastic strain rate is given by $\dot{\varepsilon}_{ij}^p = \dot{\lambda}\sigma'_{ij}$, where $\dot{\lambda}$ is a scalar coefficient and can be determined by solving the boundary value problem. The outer surface is traction free.

The above diffusion and elastic-perfectly plastic model is numerically implemented in the finite element package ABAQUS. The Li and stress−strain fields are solved with an implicit, coupled temperature-displacement procedure in ABAQUS/Standard. That is, the normalized concentration is surrogated by temperature and the lithiation expansion coefficient β_{ij} is equivalently treated as the thermal expansion coefficient. The user material subroutine for heat transfer (UMATHT) is programmed to interface with ABAQUS to update diffusivities based on the current Li concentration (i.e., temperature). The Li distribution and accordingly elastic-plastic deformation are updated incrementally. The axis-symmetric condition is used to reduce the computational cost. We choose the lithiation parameters typical for Si, $\beta_{11} = \beta_{22} = \beta_{33} = 0.6$, $\sigma_Y = 1.5$ GPa, $v = 0.3$. The diffusion properties are assigned to generate a numerically stable core−shell structure, $\Omega = 1.95$ and $I_0 = 10D_0$.

For numerical stability, the maximum of D is capped at $10^4 D_0$. More details about the simulation results are included in the Supporting Information.

Supporting Information Available: Experimental setup and other supporting figures of chemical lithiation, details of the mechanics model and finite element simulation, and discussion of the tensile hoop stress reversing the initial compression during the SiNP lithiation; videos as described in the text. This material is available free of charge *via* the Internet at http://pubs.acs.org.

REFERENCES AND NOTES

1. Arico, A. S.; Bruce, P.; Scrosati, B.; Tarascon, J. M.; Van Schalkwijk, W. Nanostructured Materials for Advanced Energy Conversion and Storage Devices. *Nat. Mater.* **2005**, *4*, 366–377.

2. Tarascon, J.-M. Key Challenges in Future Li-Battery Research. *Phil Trans. R. Soc. A* **2010**, *368*, 3227–3241.

3. Liu, X. H.; Huang, J. Y. *In Situ* TEM Electrochemistry of Anode Materials in Lithium Ion Batteries. *Energy Environ. Sci.* **2011**, *4*, 3844–3860.

4. Yao, Y.; McDowell, M. T.; Ryu, I.; Wu, H.; Liu, N. A.; Hu, L. B.; Nix, W. D.; Cui, Y. Interconnected Silicon Hollow Nanospheres for Lithium-Ion Battery Anodes with Long Cycle Life. *Nano Lett.* **2011**, *11*, 2949–2954.

5. Kasavajjula, U.; Wang, C. S.; Appleby, A. J. Nano- and Bulk-Silicon-Based Insertion Anodes for Lithium-Ion Secondary Cells. *J. Power Sources* **2007**, *163*, 1003–1039.

6. Obrovac, M. N.; Christensen, L. Structural Changes in Silicon Anodes During Lithium Insertion/Extraction. *Electrochem. Solid-State Lett.* **2004**, *7*, A93–A96.

7. Obrovac, M. N.; Krause, L. J. Reversible Cycling of Crystalline Silicon Powder. *J. Electrochem. Soc.* **2007**, *154*, A103–A108.

8. Liu, X. H.; Zhang, L. Q.; Zhong, L.; Liu, Y.; Zheng, H.; Wang, J. W.; Cho, J.-H.; Dayeh, S. A.; Picraux, S. T.; Sullivan, J. P.; *et al.* Ultrafast Electrochemical Lithiation of Individual Si Nanowire Anodes. *Nano Lett.* **2011**, *11*, 2251–2258.

9. Liu, X. H.; Zheng, H.; Zhong, L.; Huang, S.; Karki, K.; Zhang, L. Q.; Liu, Y.; Kushima, A.; Liang, W. T.; Wang, J. W.; *et al.* Anisotropic Swelling and Fracture of Silicon Nanowires During Lithiation. *Nano Lett.* **2011**, *11*, 3312–3318.

10. Beaulieu, L. Y.; Eberman, K. W.; Turner, R. L.; Krause, L. J.; Dahn, J. R. Colossal Reversible Volume Changes in Lithium Alloys. *Electrochem. Solid-State Lett.* **2001**, *4*, A137–A140.

11. Beaulieu, L. Y.; Hatchard, T. D.; Bonakdarpour, A.; Fleischauer, M. D.; Dahn, J. R. Reaction of Li with Alloy Thin Films Studied by *in Situ* AFM. *J. Electrochem. Soc.* **2003**, *150*, A1457–A1464.

12. Hertzberg, B.; Alexeev, A.; Yushin, G. Deformations in Si-Li Anodes Upon Electrochemical Alloying in Nano-confined Space. *J. Am. Chem. Soc.* **2010**, *132*, 8548–8549.

13. Graetz, J.; Ahn, C. C.; Yazami, R.; Fultz, B. Highly Reversible Lithium Storage in Nanostructured Silicon. *Electrochem. Solid-State Lett.* **2003**, *6*, A194–A197.

14. Magasinski, A.; Dixon, P.; Hertzberg, B.; Kvit, A.; Ayala, J.; Yushin, G. High-Performance Lithium-Ion Anodes Using a Hierarchical Bottom-up Approach. *Nat. Mater.* **2010**, *9*, 461–461.

15. Chan, C. K.; Peng, H. L.; Liu, G.; McIlwrath, K.; Zhang, X. F.; Huggins, R. A.; Cui, Y. High-Performance Lithium Battery Anodes Using Silicon Nanowires. *Nat. Nanotechnol.* **2008**, *3*, 31–35.

16. Takamura, T.; Ohara, S.; Uehara, M.; Suzuki, J.; Sekine, K. A Vacuum Deposited Si Film Having a Li Extraction Capacity over 2000 mAh/g with a Long Cycle Life. *J. Power Sources* **2004**, *129*, 96–100.

17. Cui, L. F.; Ruffo, R.; Chan, C. K.; Peng, H. L.; Cui, Y. Crystalline-Amorphous Core–Shell Silicon Nanowires for High Capacity and High Current Battery Electrodes. *Nano Lett.* **2009**, *9*, 491–495.

18. Park, M. H.; Kim, M. G.; Joo, J.; Kim, K.; Kim, J.; Ahn, S.; Cui, Y.; Cho, J. Silicon Nanotube Battery Anodes. *Nano Lett.* **2009**, *9*, 3844–3847.

19. Zhao, K.; Wang, W. L.; Gregoire, J.; Pharr, M.; Suo, Z.; Vlassak, J.; Kaxiras, E. Lithium-Assisted Plastic Deformation of Silicon Electrodes in Lithium-Ion Batteries: A First-Principles Theoretical Study. *Nano Lett.* **2011**, *11*, 2962–2967.

20. Zhao, K. J.; Pharr, M.; Vlassak, J. J.; Suo, Z. G. Inelastic Hosts as Electrodes for High-Capacity Lithium-Ion Batteries. *J. Appl. Phys.* **2011**, *109*, 016110.

21. Huang, J. Y.; Zhong, L.; Wang, C. M.; Sullivan, J. P.; Xu, W.; Zhang, L. Q.; Mao, S. X.; Hudak, N. S.; Liu, X. H.; Subramanian, A.; *et al. In Situ* Observation of the Electrochemical Lithiation of a Single SnO$_2$ Nanowire Electrode. *Science* **2010**, *330*, 1515–1520.

22. Ryu, I.; Choi, J. W.; Cui, Y.; Nix, W. D. Size-Dependent Fracture of Si Nanowire Battery Anodes. *J. Mech. Phys. Solids* **2011**, *59*, 1717–1730.

23. Liu, X. H.; Zhong, L.; Zhang, L. Q.; Kushima, A.; Mao, S. X.; Li, J.; Ye, Z. Z.; Sullivan, J. P.; Huang, J. Y. Lithium Fiber Growth on the Anode in a Nanowire Lithium Ion Battery During Charging. *Appl. Phys. Lett.* **2011**, *98*, 183107.

24. Zhang, L. Q.; Liu, X. H.; Liu, Y.; Huang, S.; Zhu, T.; Gui, L.; Mao, S. X.; Ye, Z. Z.; Wang, C. M.; Sullivan, J. P.; *et al.* Controlling the Lithiation-Induced Strain and Charging Rate in Nanowire Electrodes by Coating. *ACS Nano* **2011**, *5*, 4800–4809.

25. Zhong, L.; Liu, X. H.; Wang, G. F.; Mao, S. X.; Huang, J. Y. Multiple-Stripe Lithiation Mechanism of Individual SnO$_2$ Nanowires in a Flooding Geometry. *Phys. Rev. Lett.* **2011**, *106*, 248302.

26. Liu, Y.; Zheng, H.; Liu, X. H.; Huang, S.; Zhu, T.; Wang, J.; Kushima, A.; Hudak, N. S.; Huang, X.; Zhang, S.; *et al.* Lithiation-Induced Embrittlement of Multiwalled Carbon Nanotubes. *ACS Nano* **2011**, *5*, 7245–7253.

27. Liu, X. H.; Huang, S.; Picraux, S. T.; Li, J.; Zhu, T.; Huang, J. Y. Reversible Nanopore Formation in Ge Nanowires During Lithiation-Delithiation Cycling: An *In Situ* Transmission Electron Microscopy Study. *Nano Lett.* **2011**, *11*, 3991–3997.

28. Liu, Y.; Hudak, N. S.; Huber, D. L.; Limmer, S. J.; Sullivan, J. P.; Huang, J. Y. *In Situ* Transmission Electron Microscopy Observation of Pulverization of Aluminum Nanowires and Evolution of the Thin Surface Al$_2$O$_3$ Layers During Lithiation–Delithiation Cycles. *Nano Lett.* **2011**, *11*, 4188–4194.

29. Kushima, A.; Liu, X. H.; Zhu, G.; Wang, Z. L.; Huang, J. Y.; Li, J. Leapfrog Cracking and Nanoamorphization of ZnO Nanowires During *in Situ* Electrochemical Lithiation. *Nano Lett.* **2011**, *11*, 4535–4541.

30. Vajda, P.; Beuneu, F. Electron Radiation Damage and Li-Colloid Creation in Li$_2$O. *Phys. Rev. B* **1996**, *53*, 5335–5340.

31. Krexner, G.; Prem, M.; Beuneu, F.; Vajda, P. Nanocluster Formation in Electron-Irradiated Li$_2$O Crystals Observed by

Elastic Diffuse Neutron Scattering. *Phys. Rev. Lett.* **2003**, *91*, 135502.

32. Liu, D. R.; Williams, D. B. The Electron-Energy-Loss Spectrum of Lithium Metal. *Philos. Mag. B* **1986**, *53*, L123–L128.

33. Hatchard, T. D.; Dahn, J. R. *In Situ* XRD and Electrochemical Study of the Reaction of Lithium with Amorphous Silicon. *J. Electrochem. Soc.* **2004**, *151*, A838–A842.

34. Bhandakkar, T. K.; Gao, H. Cohesive Modeling of Crack Nucleation in a Cylindrical Electrode under Axisymmetric Diffusion Induced Stresses. *Int. J. Solids .Struct.* **2011**, *48*, 2304–2309.

35. Cheng, Y.-T.; Verbrugge, M. W. Evolution of Stress within a Spherical Insertion Electrode Particle under Potentiostatic and Galvanostatic Operation. *J. Power Sources* **2009**, *190*, 453–460.

36. Chon, M. J.; Sethuraman, V. A.; McCormick, A.; Srinivasan, V.; Guduru, P. R. Real-Time Measurement of Stress and Damage Evolution During Initial Lithiation of Crystalline Silicon. *Phys. Rev. Lett.* **2011**, *107*, 045503.

37. Gao, H. J.; Ji, B. H.; Jager, I. L.; Arzt, E.; Fratzl, P. Materials Become Insensitive to Flaws at Nanoscale: Lessons from Nature. *Proc. Natl. Acad. Sci. U.S.A.* **2003**, *100*, 5597–5600.

38. Zhu, T.; Li, J. Ultra-strength Materials. *Prog. Mater. Sci.* **2010**, *55*, 710–757.

39. Hu, Y. H.; Zhao, X. H.; Suo, Z. G. Averting Cracks Caused by Insertion Reaction in Lithium-Ion Batteries. *J. Mater. Res.* **2010**, *25*, 1007–1010.

40. McMeeking, R. M. Finite Deformation Analysis of Crack-Tip Opening in Elastic-Plastic Materials and Implications for Fracture. *J. Mech. Phys. Solids* **1977**, *25*, 357–381.

41. Sethuraman, V. A.; Chon, M. J.; Shimshak, M.; Srinivasan, V.; Guduru, P. R. *In Situ* Measurements of Stress Evolution in Silicon Thin Films During Electrochemical Lithiation and Delithiation. *J. Power Sources* **2010**, *195*, 5062–5066.

42. Liu, W. R.; Yang, M. H.; Wu, H. C.; Chiao, S. M.; Wu, N. L. Enhanced Cycle Life of Si Anode for Li-Ion Batteries by Using Modified Elastomeric Binder. *Electrochem. Solid-State Lett.* **2005**, *8*, A100–A103.

Size Dependent Fracture of Silicon Nanoparticles During Lithiation

Xiao Hua Liu,[†] Li Zhong,[‡] Shan Huang,[¶] Scott X. Mao,[‡] Ting Zhu,[*,¶] and Jian Yu Huang[*,†]

[†]Center for Integrated Nanotechnologies, Sandia National Laboratories, Albuquerque, New Mexico 87185, United States

[‡]Department of Mechanical Engineering and Materials Science, University of Pittsburgh, Pittsburgh, Pennsylvania 15261, United States

[¶]Woodruff School of Mechanical Engineering, Georgia Institute of Technology, Atlanta, Georgia 30332, United States

[*]Correspondence: jhuang@sandia.gov, ting.zhu@me.gatech.edu
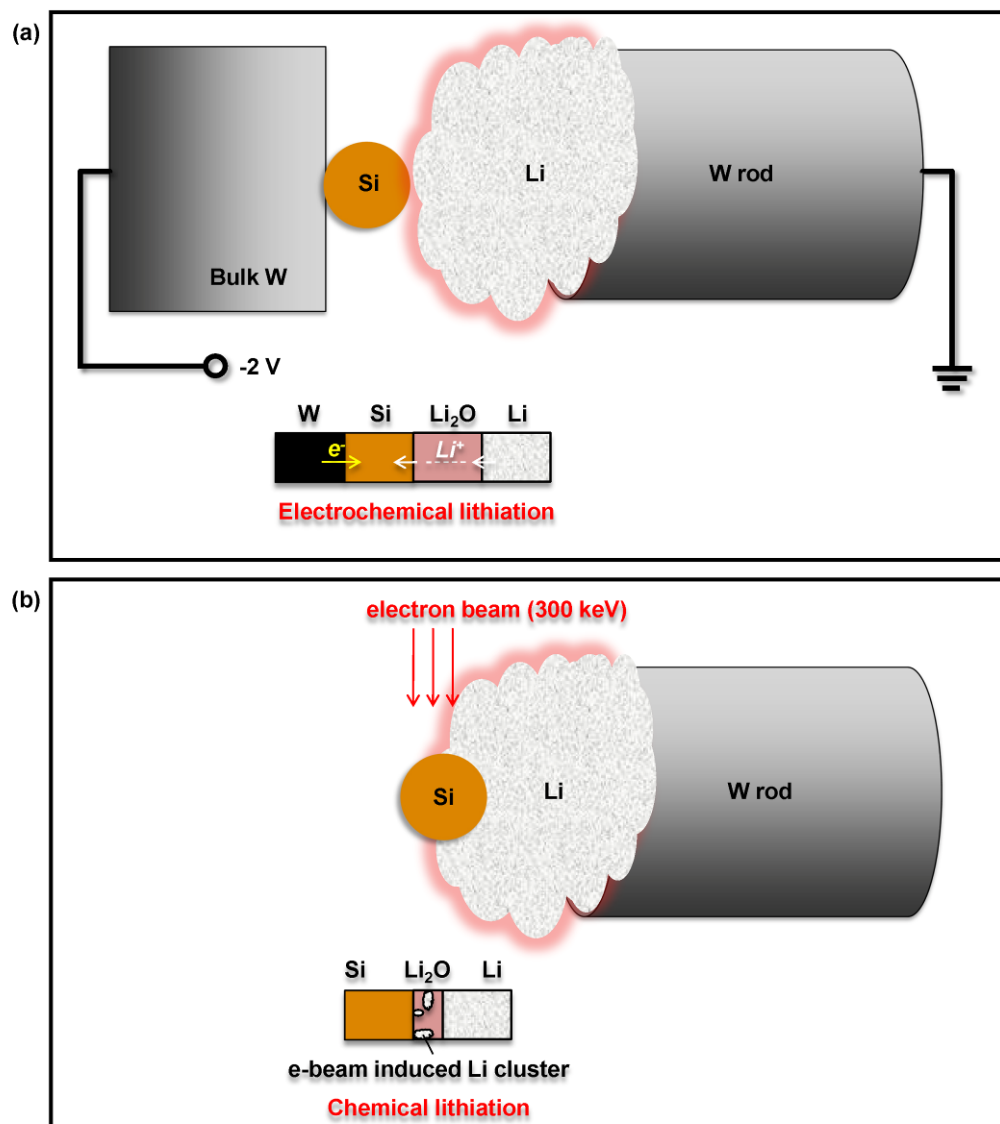
1. Supporting Figures:

Figure S1. Schematic illustration of the *in situ* lithiation of individual Si particles (SiNPs). (a) Electrochemical lithiation. Lithium metal on a tungsten (W) rod serves as the reference electrode and the lithium source. A naturally formed Li_2O layer on the Li metal is a solid-state electrolyte that allows Li^+ transport when a potential of -2 V is applied through bulk W to a single SiNP. (2) Chemical lithiation under intense electron beam, which induces Li_2O decomposition *via* $2Li_2O \rightarrow 4Li + O_2\uparrow$. Then the adjacent SiNP is lithiated by the produced elemental Li.
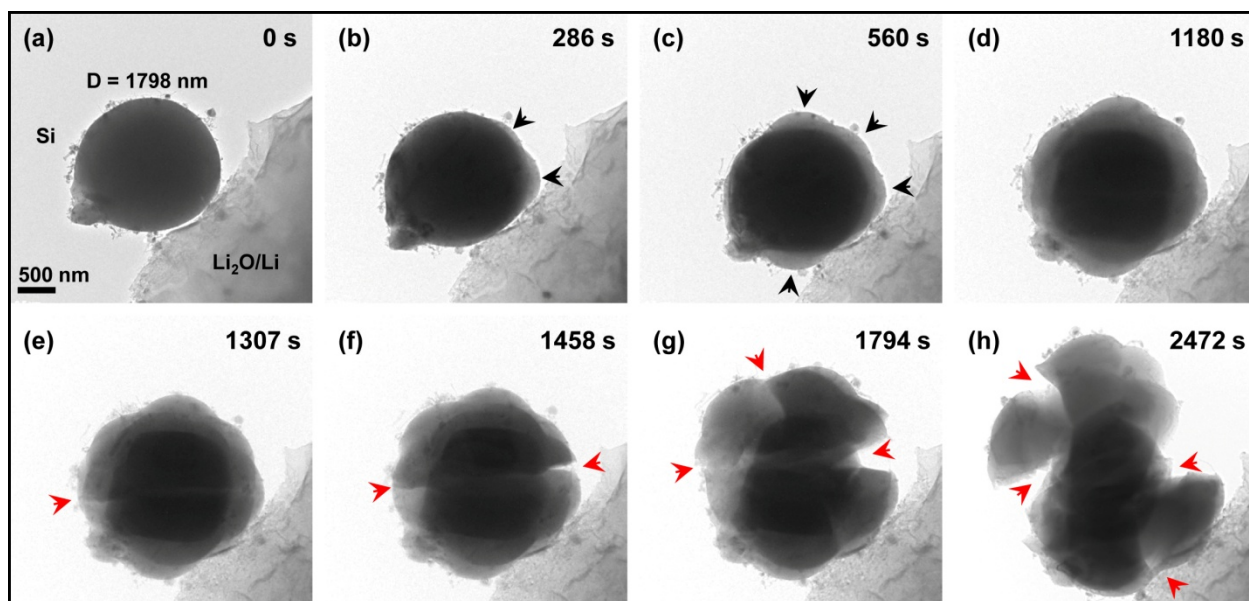
Figure S2. Cracking and fracture of a free-standing 1800-nm SiNP during chemical lithiation. (a-h) Under the irradiation of the 300 keV electron beam, Li_2O was decomposed to produce reactive Li atoms that lithiate the adjacent SiNP sitting on it. The black arrowheads mark the bumps due to anisotropic lithiation of Si in the initial stage before crack formation (b-c), while the red arrowheads mark the cracks formed in the thickened Li_xSi shell (e-h). The whole process took more than 40 minutes, but the slow lithiation did not prevent cracking and fracture from happening during the lithiation process.
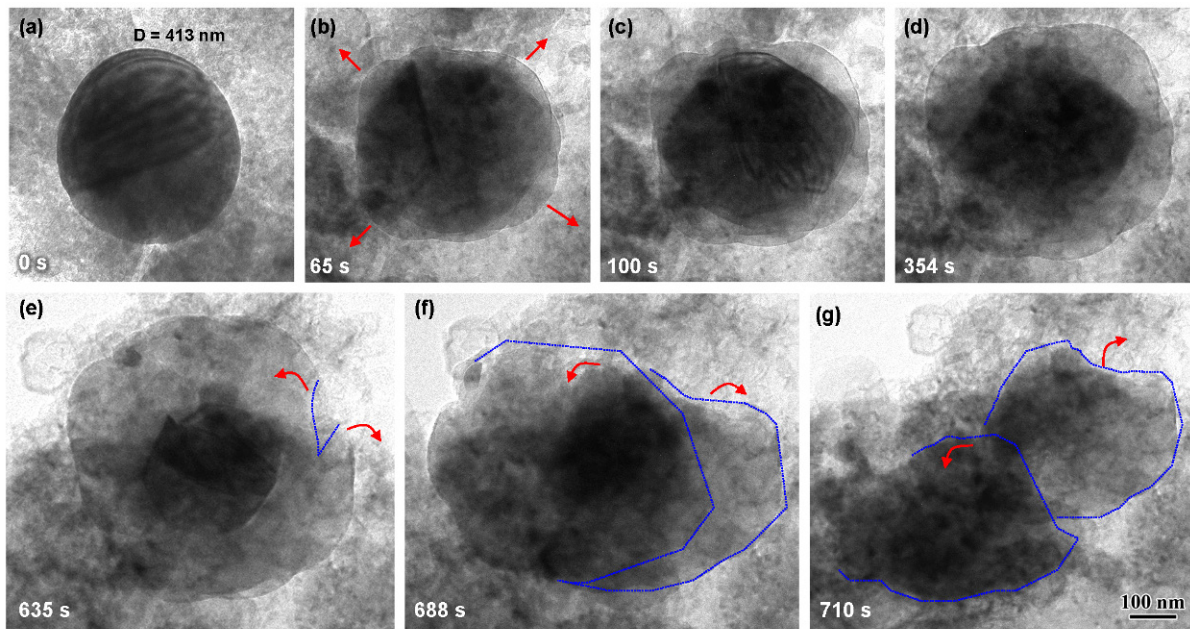
Figure S3. Fracture of a free-standing SiNP on Li_2O during the chemical lithiation. The red arrows mark the expansion direction and the blue lines mark the profile of the fractured particle.
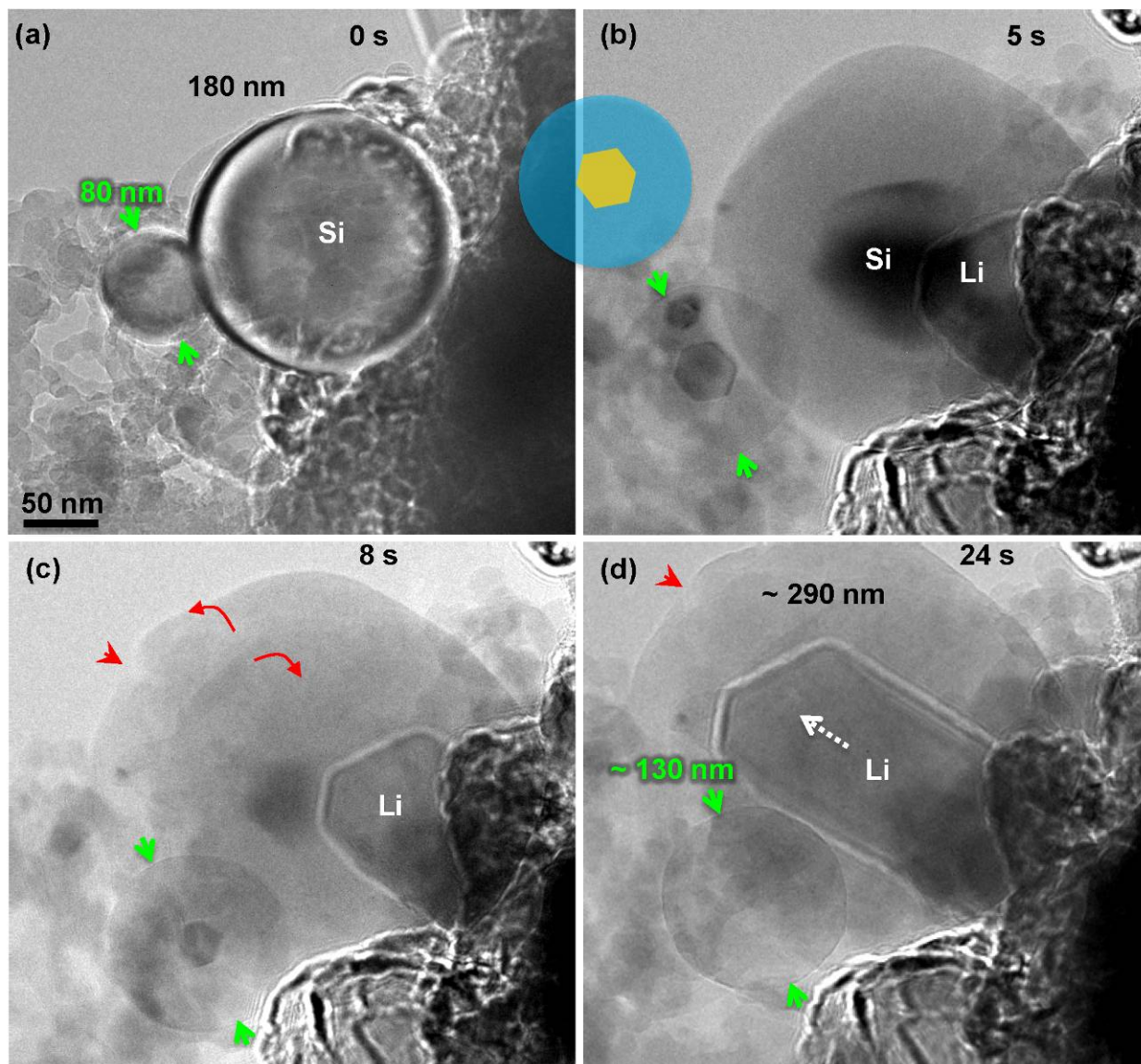
Figure S4. Chemical lithiation of two SiNPs with different diameters. (a) Pristine round SiNPs with diameters of 80 and 180 nm, respectively. (b) Core-shell structure during the lithiation. The smaller SiNP had a hexagonal core as illustrated by the cartoon. (c) Cracks (marked by the red arrows) formed when the Li$_x$Si shell was thickened. (d) Fully lithiated SiNPs with diameters of 130 and 290 nm, respectively. A Li fiber grew out under the electron beam.

2. Modeling Details

On the basis of experimental observations, we developed a model of Li diffusion and elastic-plastic deformation, simultaneously accounting for both the large plastic deformation and the evolution of a core-shell structure with coexisting Li-rich and Li-poor phases. The predicted stress distributions allowed us to explain

  (1) Why fracture first initiates from the surface?
  (2) What is the origin of the particle size effects on fracture?

2.1 Generation of Hoop Tensile Stress
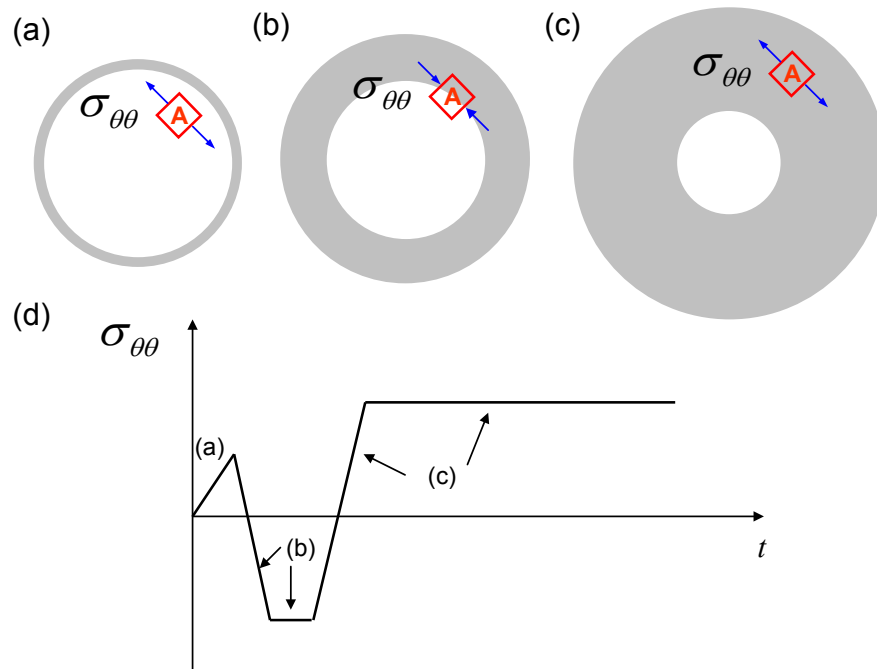
Figure S5. Illustration of how the hoop stress $\sigma_{\theta\theta}$ changes in a spherical particle with an evolving structure of pristine core (white) and lithiated shell (grey). (a-c) $\sigma_{\theta\theta}$ in a representative material element A located at various distances relative to the moving lithiation reaction front, *i.e.*, the core-shell interface. Progressive lithiation results in a gradual expansion of the particle. (d) $\sigma_{\theta\theta}$ as a function of time t in element A.

To provide a direct physical appreciation of stress generation, we show in Figures S5a-d the history of the stress experienced by a representative material element *A*. Here the lithiation reaction front was simplified as a sharp interface between the shrinking pristine core (white) and growing lithiated shell (grey). The shell was assumed to be fully lithiated. This implies that Li diffusion is extremely fast in the lithiated shell, *i.e.*, the propagation of the reaction front is the rate limiting step, as indicated by our measurements of the linear time dependence of reaction front migration distance in lithiated Si nanowires.[1] To focus on essential ideas, we assumed that the lithiation strain induced by the electrochemical reaction of Li insertion is dilatational and equal in all directions, *e.g.*, (r,θ,φ) directions in a spherical coordinate system. This lithiation strain is accommodated by subsequent elastic-plastic deformation, dictated by the stress equilibrium of deformable bodies.

In Figure S5d, the hoop stress versus time curve indicates that during progressive lithiation, the hoop stress $\sigma_{\theta\theta}$ in element *A* sequentially undergoes elastic tension (Figure S5a), compressive plastic yielding (Figure S5b), elastic unloading and reverse tensile plastic yielding (Figure S5c), all occurring in a single lithiation process. It is the last stage of large tensile hoop stress that dominates in the surface layer for most of time as the lithiation front propagates towards the center, providing the main driving force of fracture in nanoparticles during Li insertion.

More specifically, Figure S5a shows that in the early stage of lithiation, element *A* is located within the pristine core. As lithiation occurs at the reaction front, the newly lithiated material at the front tends to expand more in the outward radial direction than in the inward radial direction. Such asymmetric expansion arises because there are larger areas in the hoop direction at larger radial distances, where the lithiation-induced volume expansion can be better accommodated with lower stresses generated. The dominant outward displacement of newly lithiated materials results in hydrostatic tension in element *A*, as represented by stage (a) of the $\sigma_\theta - t$ curve in Figure S5d. As the reaction front sweeps through element *A*, a large dilatational lithiation strain is created at *A*. Due to the constraint of surrounding materials, local compressive stresses develop, such that element *A* sequentially undergoes tensile elastic unloading, compressive

elastic loading, and compressive plastic yielding in the hoop direction. This stress sequence is schematically represented by stage (b) in Figure S5d. Interestingly, as the reaction front continues to move toward the center, the lithiation strain newly created at the front causes further displacements of element A in the outward radial direction and simultaneously stretches it in the hoop directions (both θ and φ). As a result, element A experiences compressive elastic unloading, tensile elastic loading, and tensile plastic yielding, which correspond to stage (c) in Figure S5d. It is important to note that the large tensile hoop stress in the surface layer could cause fracture of nanoparticles as shown in our *in situ* TEM experiments.

2.2 Simulation of Stress Generation

To gain further insights into the stress development during lithiation, we have simulated the co-evolving processes of lithium diffusion and stress generation. The time evolution of the two Li phases is modeled by using a non-linear diffusion model. The concentration of Li, c, is governed by the standard diffusion equation. It is normalized by the Li concentration at the fully lithiated state, such that c varies between 0 and 1. To capture the co-existence of Li-poor and Li-rich phases, we assume that the diffusivity D is non-linearly dependent on c. Note that our diffusion simulations mainly serve to generate a sequence of core-shell structures for the stress analyses, rather than provide a precise description of the dynamic lithiation process that would be difficult due to lack of experimental measurements for model calibration. To this end, we take a simple non-linear function

$$D = D_0\left[1/(1-c) - 2\Omega c\right] \qquad (1)$$

where D_0 is the diffusivity constant and Ω is tuned to control the concentration profile near the reaction front. On the basis of the free energy function of a regulation solution model, $f = \Omega c(1-c) + \left[c\ln c + (1-c)\ln(1-c)\right]$, diffusivity D in Eq. (1) is derived according to a definition that can sharply increase diffusivities at high Li concentrations, $D = -D_0 c\, d^2 f / dc^2$. In diffusion simulations, the normalized Li concentrations behind the reaction front can quickly attain the high values (slightly below 1), while those ahead of the front remain nearly zero. This

produces a sharp reaction front that is consistent with experimental observation, thereby providing a basis of further stress analysis. It should be noted that a small gradient of lithium concentration still exists behind the reaction front, so that Li can diffuse through the lithiated shell continuously to reach and move forward the reaction front toward the center of the particle. Finally, we emphasize again that the non-linear diffusivity function in Eq. (1) is entirely empirical, and taken as a numerical convenience for generating the sharp phase boundary for stress analyses. The mechanically based model is needed to describe the motion of phase boundary and Li diffusion in each phases in the future study. The particle is initially pristine and subjected to a constant Li flux I_0 at the surface.

We adopt an elastic and perfectly plastic model to describe the lithiation-induced deformation. The total strain rate, $\dot{\varepsilon}_{ij}$, is taken to be the sum of three contributions

$$\dot{\varepsilon}_{ij} = \dot{\varepsilon}_{ij}^c + \dot{\varepsilon}_{ij}^e + \dot{\varepsilon}_{ij}^p \tag{2}$$

where $\dot{\varepsilon}_{ij}^c$ is the chemical strain rate caused by lithiation and is proportional to the rate of the normalized lithium (Li) concentration $\dot{c}$,

$$\dot{\varepsilon}_{ij}^c = \beta_{ij}\dot{c} \tag{3}$$

where β_{ij} is the lithiation expansion coefficient and c varies between 0 (*e.g.*, pristine Si) and 1 (*e.g.*, fully lithiated Li$_{3.75}$Si). In Eq. (2), $\dot{\varepsilon}_{ij}^e$ denotes the elastic strain rate and obeys Hooke's law

$$\dot{\varepsilon}_{ij}^e = \frac{1}{E}\left[(1+v)\dot{\sigma}_{ij} - v\dot{\sigma}_{kk}\delta_{ij}\right] \tag{4}$$

where E is Young's modulus, v is Poisson's ratio, $\delta_{ij} = 1$ when $i = j$ and $\delta_{ij} = 0$ otherwise, repeated indices mean summation. In Eq. (2), the plastic strain rate, $\dot{\varepsilon}_{ij}^p$, obeys the classic J_2-flow rule. That is, plastic yielding occurs when the von Mises equivalent stress, $\sigma_{eq} = \sqrt{3\sigma_{ij}'\sigma_{ij}'/2}$, equals the yield strength σ_Y, where $\sigma_{ij}' = \sigma_{ij} - \sigma_{kk}\delta_{ij}/3$ is the deviatoric stress. The plastic strain rate is given by

$$\dot{\varepsilon}_{ij}^{p} = \dot{\lambda}\sigma_{ij}' \qquad\qquad (5)$$

where $\dot{\lambda}$ is a scalar coefficient and can be determined by solving the boundary value problem. The outer surface is traction free.

The above diffusion and elastic-perfectly plastic model is numerically implemented in the finite element package ABAQUS 6.10. The Li and stress-strain fields are solved with an implicit, coupled temperature-displacement procedure in ABAQUS/Standard. That is, the normalized concentration is surrogated by temperature and the lithiation expansion coefficient β_{ij} is equivalently treated as the thermal expansion coefficient. The user material subroutine for heat transfer (UMATHT) is programmed to interface with ABAQUS to update diffusivities based on the current Li concentration (*i.e.*, temperature). The Li distribution and accordingly elastic-plastic deformation are updated incrementally. The axis-symmetric condition is used to reduce the computational cost. We choose the lithiation parameters typical for Si, $\beta_{11} = \beta_{22} = \beta_{33} = 0.6$, $\sigma_{Y} = 1.5$ GPa, $v = 0.3$. The diffusion properties are assigned to generate a numerically stable core-shell structure, $\Omega = 1.95$ and $I_0 = 10D_0$. For numerical stability, the maximum of D is capped at $10^4 D_0$.

Figure S6 shows the simulation results of Li and stress distributions during lithiation, additional to Fig. 7c in the text. It is seen that the Li concentration profiles capture the juxtaposition of the Li-poor and Li-rich phases. The interface between the pristine core and lithiated shell can be identified approximately at the radial distance where the Li concentration has an abrupt change. In addition, c transits smoothly to the limits of 0 and 1 near the reaction interface, thereby facilitating numerical stability. As Li continuously fluxes in from the surface, the reaction front moves toward the center. Because of the spherical symmetry, the hoop stresses $\sigma_{\theta\theta} = \sigma_{\varphi\varphi}$ and all the shear stresses vanish. Figures S6b-d show the radial stress distributions, which respectively correspond to the three Li concentration profiles in Fig. S6a. Of particular importance is the insights gained from the combined reading of the radial distributions of $\sigma_{\theta\theta}$ and σ_{Mises} in Fig. S6d. Namely, material elements at the increasing radial distance r experience the respective hoop stress of (hydrostatic) tension, compressive plastic yielding, elastic unloading, tensile elastic

10

loading, and tensile plastic yielding. This spatial stress variation can be directly correlated to the schematic plot in Figure S5d showing the temporal evolution of $\sigma_{\theta\theta}$ at a fixed material element.
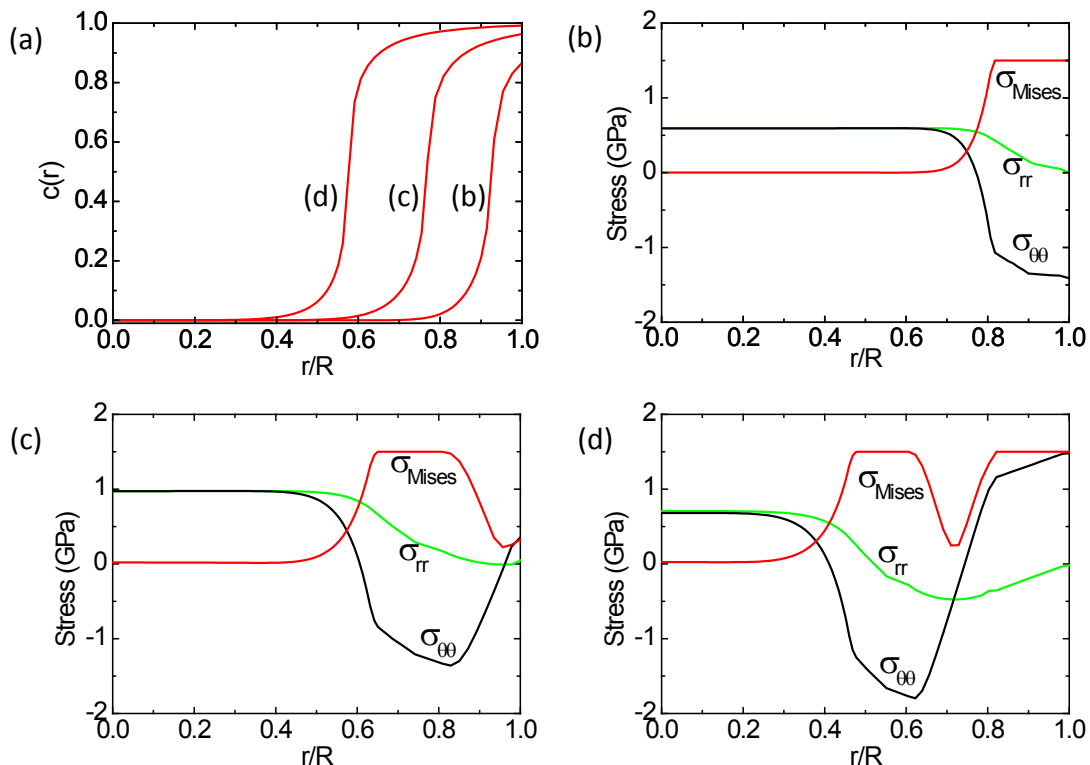

Figure S6. The Li and stress distributions in a spherical particle. (a) Li concentration c versus radial distance r at different moments, (b) → (c) → (d). Here c is normalized by its maximum value at the fully lithiated state, and r is normalized by the current radius R of a partially lithiated particle (R increases as lithiation proceeds). (b-d) Radial distribution of stresses corresponding to different Li concentration profiles in (a).

Note that we have solved the same mechanics problem of lithiation-induced stresses with a semi-analytic solution and finite difference numerical procedure. The mechanics foundation is more transparent in this semi-analytic model. The corresponding numerical results of stress generation are consistent with those from finite element, thus providing a solid mathematical support to our theoretical analysis. Since this semi-analytic model involves the long mathematic formulas, we feel it is more suited to a mechanics oriented journal and will prepare a manuscript for a separate submission.

2.3 Size Effect on Fracture

To study the size effect on fracture in lithiated Si nanoparticles, we note that while the materials in the surface layer experience a complicated deformation history, Figure S5d, the large tensile stresses dominate and persist for most of the progressive lithiation process. As a result, the non-linear fracture mechanics approach of *J*-integral can be utilized approximately to evaluate the size effect on the energy release rate of crack extension.
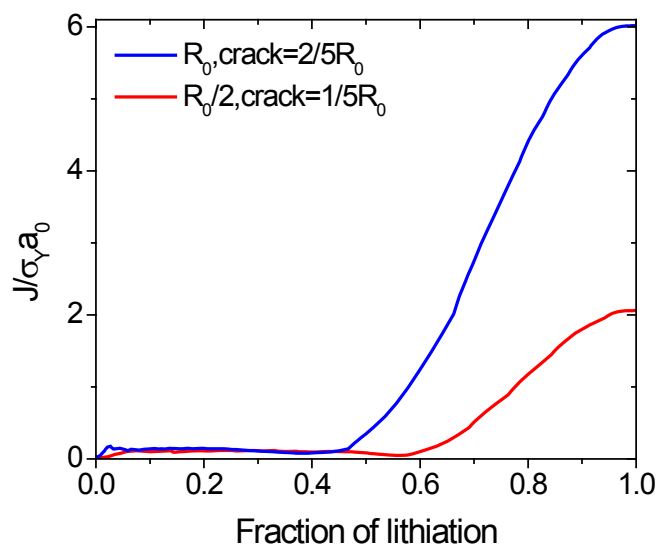

Figure S7. *J*-integral near the crack tip as a function of fraction of lithiation. The same ratio of crack length to radius is used for both large and small cross sections.

To evaluate *J*-integral, we used a quasi two-dimensional geometry of a cylindrical wire with a surface crack of size a. Along the same line as the particle, we performed the simulations of Li diffusion and elastic-plastic deformation. The evolution and distribution of stress in the cross section of the wire is similar to that of a particle. We considered initial radii of R_0 and $R_0/2$, and the crack length $a = 0.1R_0$. The *J*-integral on the contour near the crack tip was used as an effective measure of driving force of crack extension when irreversible deformation is involved. Figure 7e in the text plots the calculated values of *J*-integral as a function of the fraction of lithiation, defined as the ratio between the thicknesses of the lithiated shell to the current radius

of the circle. The maximum of J-integral, J_{max}, corresponds to a complete lithiation. The critical size of fracture is determined by the condition of J_{max} equal to surface energy 2γ. Figure 7e in the text clearly shows the particle size effects on the energy release rate. In addition, Figure S7 shows the J-integral curves for both large and small cross sections with the same ratio of crack length to radius. A significant particle size effect is also clearly seen. However, a quantitative prediction of the critical size requires quantitative material parameters, *e.g.*, Young's modulus, yield stress, strain hardening/softening exponent, *etc.*, all of which can depend strongly on the level of lithiation and most of which have not been reported in the literature. Nevertheless, our modeling reveals the mechanistic origin of tensile stress generation in the lithiated surface layer as well as the particle size effect, providing a framework of further study for averting fracture in lithiated particle electrodes.

References:

(1)   Liu, X. H.; Zheng, H.; Zhong, L.; Huang, S.; Karki, K.; Zhang, L. Q.; Liu, Y.; Kushima, A.; Liang, W. T.; Wang, J. W.; Cho, J.-H.; Epstein, E.; Dayeh, S. A.; Picraux, S. T.; Zhu, T.; Li, J.; Sullivan, J. P.; Cumings, J.; Wang, C.; Mao, S. X.; Ye, Z. Z.; Zhang, S.; Huang, J. Y. *Nano Lett.* **2011,** 11 (8), 3312-3318.